Non-thermal emission from the plunging region: a model for the high-energy tail of black hole X-ray binary soft states

Amelia M. Hankla [1,2]★† Nicolas Scepi [1] and Jason Dexter [1,3]

[1]*JILA, University of Colorado and National Institute of Standards and Technology, 440 UCB, Boulder, CO 80309-0440, USA*
[2]*Department of Physics, University of Colorado, 390 UCB, Boulder, CO 80309-0390, USA*
[3]*Department of Astrophysical and Planetary Sciences, University of Colorado, 391 UCB, Boulder, CO 80309, USA*

ABSTRACT

X-ray binaries exhibit a soft spectral state comprising thermal blackbody emission at 1 keV and a power-law tail above 10 keV. Empirical models fit the high-energy power-law tail to radiation from a non-thermal electron distribution, but the physical location of the non-thermal electrons and the reason for their power-law index and high-energy cut-off are still largely unknown. Here, we propose that the non-thermal electrons originate from within the black hole's innermost stable circular orbit (the 'plunging region'). Using an analytic model for the plunging region dynamics and electron distribution function properties from particle-in-cell simulations, we outline a steady-state model that can reproduce the observed spectral features. In particular, our model reproduces photon indices of $\Gamma \gtrsim 2$ and power-law luminosities of the order of a few per cent of the disc luminosity for strong magnetic fields, consistent with observations of the soft state. Because the emission originates so close to the black hole, we predict that the power-law luminosity should strongly depend on the system inclination angle and black hole spin. This model could be extended to the power-law tails observed above 400 keV in the hard state of X-ray binaries.

Key words: acceleration of particles – accretion, accretion discs – black hole physics – X-rays: binaries.

1 INTRODUCTION

Observations of accreting black hole X-ray binary systems (XRBs) show two main X-ray spectral states. The hard state has an inverted power-law photon spectrum $N(E) \propto E^{-\Gamma}$ with a spectral index $\Gamma \lesssim 2$ at 10 keV, peaking in the 100–200 keV range. The soft state has a thermal blackbody component peaking around 1 keV and a high-energy power-law tail component from 10 keV to 1 MeV. This hard X-ray to soft gamma-ray power law has a spectral index $\Gamma \gtrsim 2$ and no observed cut-off (McConnell et al. 2002; Zdziarski & Gierlinski 2004; Remillard & McClintock 2006).

Models of the soft spectral state usually involve a thin accretion disc that produces the thermal emission and a hot, optically thin gas that produces the high-energy power-law tail. The thin accretion disc (Novikov & Thorne 1973; Shakura & Sunyaev 1973) models the soft state's blackbody emission well. However, the origin of the power-law tail is less well understood. Most models for the power-law tail assume a population of non-thermal electrons that are somehow accelerated to high energies, presumably by shocks or magnetic reconnection. The hybrid thermal/non-thermal electron distribution function fits the soft state spectrum up to 600 keV well (Gierliński et al. 1999; Zdziarski et al. 2001), but the electron distribution parameters are determined by the best fit to observational data rather than ab initio theory.

The spatial location of the hot, optically thin gas and thus the non-thermal electrons is unknown. Hybrid electron distribution models usually assume that the non-thermal electrons originate from a jet or corona above a thin accretion disc extending down to the innermost stable circular orbit (ISCO; Zdziarski & Gierlinski 2004). Alternatively, the non-thermal electrons could come from gas within the ISCO. In the 'plunging region', particle orbits transition from predominantly circular to predominantly radial. The ISCO serves as an artificial boundary condition in early thin disc models, which assume that the stress there goes to zero and no light is emitted from within the plunging region (Novikov & Thorne 1973; Shakura & Sunyaev 1973). Later, thin disc models find that stress at the ISCO can lead to extra dissipation, which is often parametrized as an additional accretion efficiency $\Delta\epsilon$ (Gammie 1999; Agol & Krolik 2000). Magnetohydrodynamic (MHD) and general relativistic MHD (GRMHD) simulations have measured additional dissipation within the ISCO of the order of $\Delta\epsilon \gtrsim 0.2$ for weakly magnetized discs and up to twice the Novikov–Thorne efficiency for strongly magnetized discs (Armitage, Reynolds & Chiang 2001; Shafee et al. 2008; Noble, Krolik & Hawley 2009; Penna et al. 2010; Avara, McKinney & Reynolds 2016). This extra dissipation could come from magnetic reconnection and turbulence occurring in the plunging region.

Extra dissipation from within the plunging region could cause the soft state's high-energy power-law tail. In a purely thermal model, the gas temperature rises so rapidly towards the event horizon that the Wien peaks sum to a power law (Zhu et al. 2012). This model could also explain high-frequency quasi-periodic oscillations in the steep power-law state (Dexter & Blaes 2014). These models assume that the electron and proton gas are in thermal equilibrium. However,

★ E-mail: amelia.hankla@colorado.edu
† National Science Foundation Graduate Research Fellow.
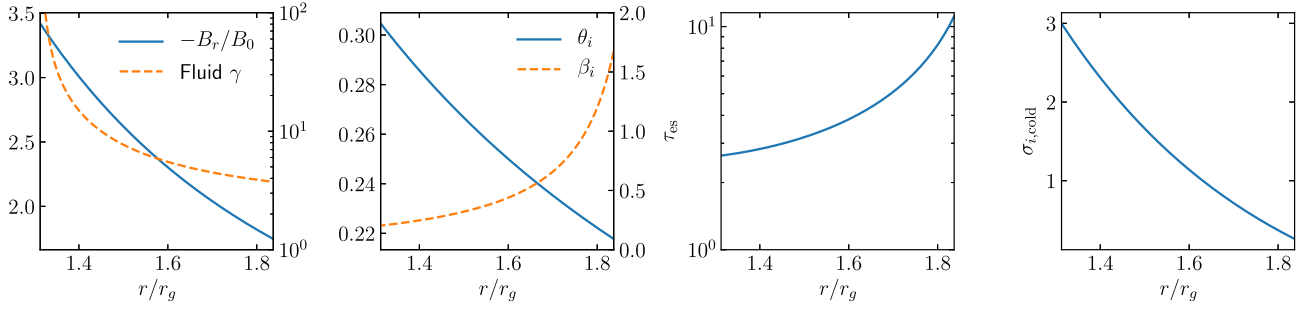
Figure 1. Properties of the plunging region calculated from the Gammie (1999) background for fiducial parameters $a = 0.95$ and $\Delta\epsilon = 1.04$. From left to right: radial magnetic field strength B_r (left axis) and the fluid's Lorentz factor (right axis), dimensionless ion temperature $\theta_i = k_B T_i / m_p c^2$ (left axis) and ratio of gas-to-magnetic pressure $\beta_i = 8\pi n_0 k_B T_i / B_r^2$ (right axis), electron scattering optical depth τ_{es}, and cold ion magnetization σ_i. Here, $B_0 = 10^8$ G. The plunging region extends from the ISCO at $1.94 r_g$ to the event horizon at $1.31 r_g$ in the mid-plane.

shorter infall times in the plunging region can mean electrons and protons no longer have time to thermalize. Estimates of the electron–proton thermalization time in GRMHD simulations become shorter than the infall time close to the black hole, suggesting that electrons and protons may decouple into a two-temperature plasma within the ISCO (Zhu et al. 2012).

In this work, we present a model for the soft spectral state's high-energy power-law tail using non-thermal electrons in the plunging region. We outline the parameter space where electron–proton decoupling should occur and demonstrate that the plunging region conditions are conducive to accelerating electrons to non-thermal energies (Section 2). We then propose a model for the hybrid thermal/non-thermal electron distribution in the plunging region based on particle acceleration prescriptions from particle-in-cell (PIC) simulations (Section 3). We show that our model can reproduce observational characteristics of a high-energy power-law tail for highly magnetized parameters, recover the transition to thermal-dominated spectra at lower magnetizations, and predict trends with inclination angle and black hole spin that are consistent with current observations (Section 4). We end by discussing our model assumptions and its general applicability to XRBs (Section 5) and summarizing our findings (Section 6).

2 DYNAMICAL MODEL FOR THE PLUNGING REGION

Within the ISCO, the accretion flow cannot be described as a thin disc. Particle orbits transition from mostly circular outside the ISCO to mostly radial inside the ISCO. The fast infall times in the plunging region mean that the usual assumptions of a collisional, single-temperature plasma need to be revisited. In this section, we will motivate our treatment of the plunging region as a two-temperature, highly magnetized region with the potential to continuously accelerate particles to non-thermal energies.

We will use Gammie (1999)'s plunging region model as a backdrop for our model. Gammie (1999) provides radial profiles of the gas number density n_0, four-velocity u^μ, and radial magnetic field strength B_r that agree well with numerical simulations (Penna et al. 2010). The model assumes a one-dimensional, steady-state MHD inflow in the plunging region, parametrized by black hole spin a, mass M, and the $F_{\theta\phi}$ component of the Maxwell tensor, which reduces to $-r^2 B_r$ at the mid-plane in the non-relativistic limit. Throughout, we assume an Eddington factor $\eta = 0.1 = L_{Edd}/(\dot{M}_{Edd} c^2)$, where L_{Edd} and $\dot{M}_{Edd}$ are the Eddington luminosity and accretion rate, respectively. We avoid numerical artefacts due to the boundary

condition $v^r = 0$ at the ISCO by starting our solutions at $r_{ISCO} - 0.1 r_g$. We scale the model to physical units using a black hole mass of $10 M_\odot$ and a density scale height $H/r = 1$, the latter choice motivated by Section 2.1's observation that ions will not collide with electrons in the plunging region.

For our fiducial model, we use values $a = 0.95$ and $F_{\theta\phi} = 6.0$, which corresponds to an accretion efficiency $\Delta\epsilon = 1.04$. For all models, we assume that $\Delta\epsilon$ is uniformly distributed throughout the volume within the ISCO and that this heating comes from magnetic reconnection processes. Representative quantities of the fiducial background are plotted in Fig. 1. For these parameters, the magnetic field has a strength of the order of 10^8 G. We assume a virial ion temperature $T_i = 2GM m_p / 5 k_B r$, which gives mildly relativistic ions, and calculate the ion beta $\beta_i = 8\pi n_0 k_B T_i / B_r^2$. The electron scattering optical depth $\tau_{es} = n_0 \sigma_T H$ is always slightly greater than 1. The values of B_r, τ, and β_i vary by a factor of ~ 3 from the ISCO to the event horizon.

2.1 Development of a two-temperature plasma

Analytic models of a thin disc that permits non-zero stress at the ISCO predict a factor of 10 increase in the gas temperature between the ISCO and the event horizon (Agol & Krolik 2000). Single-temperature GRMHD simulations find a similar increase (Zhu et al. 2012) due to the flow becoming effectively optically thin. The rapid rise of temperature means that the time-scale for electrons and protons to reach thermal equilibrium increases as well. This electron–ion thermalization time-scale t_{th}^{ei} is given by

$$\frac{dT_e}{dt} = \frac{T_i - T_e}{t_{th}^{ei}}, \tag{1}$$

where $t_{th}^{ei} \equiv 1/\nu_{th}$. For hot protons heating electrons, the thermalization frequency from Stepney & Guilbert (1983) reads

$$\nu_{th} = \frac{m_e}{m_p} \frac{n_0 \sigma_T c \ln\Lambda}{K_2(1/\theta_e) K_2(1/\theta_i)} \tag{2}$$

$$\left[\frac{2(\theta_e + \theta_i)^2 + 1}{\theta_e + \theta_i} K_1\left(\frac{\theta_e + \theta_i}{\theta_e \theta_i}\right) + 2K_0\left(\frac{\theta_e + \theta_i}{\theta_e \theta_i}\right) \right] \text{ s}^{-1} \tag{3}$$

$$= 3.6 \times 10^{-37} \frac{(m_e m_p)^{1/2} n_0 \ln\Lambda}{(m_p T_e + m_e T_i)^{3/2}} \text{ s}^{-1}, \tag{4}$$

where $\theta_e = k_B T_e / m_e c^2$ and $\theta_i = k_B T_i / m_p c^2$, m_e and m_p are electron and proton masses, respectively. The last line takes the non-relativistic limit assuming $\theta_e \ll 1$ and $\theta_i \ll 1$ (Spitzer 1956). Here, $K_0(x)$, $K_1(x)$, and $K_2(x)$ are modified Bessel functions of the second kind. Throughout, we set the Coulomb logarithm $\ln\Lambda = 10$ and employ cgs units.
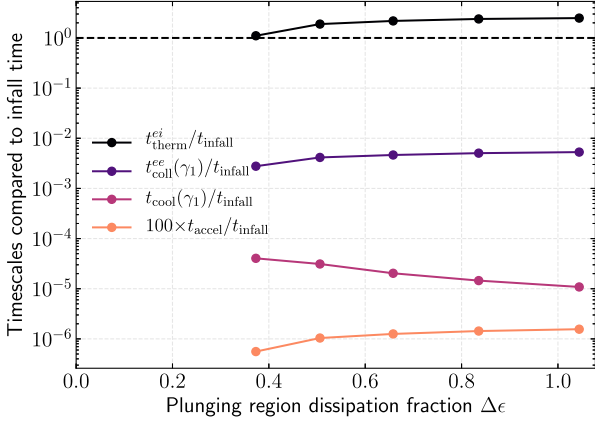
Figure 2. Time-scales in the plunging region show that all physical processes except for electron-ion collisions are fast compared to the infall time for a wide range of accretion efficiencies $\Delta\epsilon$, consistent with the hierarchy $t_{\text{accel}} \ll t_{\text{cool}}(\gamma) \ll t_{\text{coll}}^{ee}(\gamma) \ll t_{\text{infall}} \lesssim t_{\text{therm}}^{ei}$. Time-scales are shown at a radius $r = 1.58r_g$ for black hole spin $a = 0.95$. These time-scales are calculated for thermal ion and hybrid electron distributions determined by the steady-state model described in Section 3.

In the plunging region, the thermalization time-scale can become longer than the accretion time-scale. Zhu et al. (2012) find that a weakly magnetized flow cannot equilibrate within $3\,r_g$ for black hole spin $a = 0.7$. Therefore, the assumption that electrons and protons couple efficiently no longer applies within the ISCO. The inefficient Coulomb coupling means that protons cannot cool, and should heat due to viscous and magnetic dissipation. Such increased temperature and thus increased ion pressure support will puff up the plunging region beyond a thin disc. The formation of a thick inner disc and a thin outer disc was recently simulated for the first time (Liska et al. 2022). For those model parameters, the thin outer disc with $H/r \sim 10^{-2}$ expanded to $H/r \sim 0.3$ within the ISCO.

This decoupling motivates our subsequent treatment of the electrons and protons in the plunging region as completely independent, with different temperatures, as well as our assumption that $H/r \sim 1$. Indeed, Fig. 2 shows that in our model, the thermalization time (black solid line) is longer than the infall time (dashed horizontal line) for a wide range of accretion efficiencies. The same hierarchy holds for all black hole spins discussed in this work.

2.2 Non-thermal particle acceleration

PIC simulations of magnetic reconnection have shown that efficient particle acceleration in an electron-ion plasma occurs for ion magnetizations $\sigma_i \gtrsim 1$ (Werner et al. 2018). Using background profiles for magnetic field and gas density from Gammie (1999), we will demonstrate that efficient particle acceleration is possible inside the ISCO. We calculate the ion magnetization

$$\sigma_i = \frac{B_0^2}{4\pi n_0 m_p c^2} \tag{5}$$

using the definition from Werner et al. (2018). We set $B_0 = B_r$ and $n_0 = \rho/m_p$, with the radial magnetic field $B_r(r)$ and mass density $\rho(r)$ obtained from Gammie (1999). For fiducial model parameters, the ion magnetization ranges from 0.2 to 3.0 (Fig. 1). In PIC simulations of magnetic reconnection with similar ion magnetizations, Werner et al. (2018) find that electrons are accelerated into power-law distribution with high-energy cut-off $\gamma_c \sim 4\sigma_e$ (rising slowly with σ_i) and power-

law index p prescribed by

$$p = 1.9 + 0.7/\sqrt{\sigma_i}. \tag{6}$$

Werner et al. (2018) fix $\theta_i = \sigma_i/200$ (i.e. $\beta_i = 4\theta_i/\sigma_i \to 0.02$), a factor of 10 to 100 times colder than the equipartition ion temperature calculated above. PIC studies of electron-ion turbulence (rather than magnetic reconnection) that set $\beta_i = 2/3$ and scanned $\theta_i \in [1/256, 10]$ with $\sigma_i \in [1/256, 10]$ have found broadly similar power-law indices (Zhdankin et al. 2019). The turbulent simulations in general find more efficient particle acceleration, measuring $p \approx 2.8$ for $\theta_i = 1/16$ and $\sigma_i = 0.2$ when equation (6) would predict $p = 3.5$.

With ion magnetizations close to unity, the plunging region can plausibly accelerate electrons to non-thermal energies via turbulence or reconnection. This acceleration could happen in a two-stage process, with sharp increases in particle Lorentz factor when the particle crosses a current sheet and slower, second-order Fermi-like acceleration that continues to increase particle energy over time (Comisso & Sironi 2019). For a magnetically dominated pair plasma, the current sheet acceleration time is of the order of $t_{\text{acc}} \sim (300/\sigma)\omega_{pe}^{-1}$ (Comisso & Sironi 2019), where $\omega_{pe} = \sqrt{4\pi e^2 n_0/m_e}$ is the electron plasma frequency. For the fiducial parameters $\Delta\epsilon = 1.04$ and $a = 0.95$, the Gammie (1999) model yields $100\omega_{pe}^{-1} \sim 10^{-11}$ s, much shorter than infall times of the order of 10^{-4} s for a 10 solar-mass black hole and electron-ion thermalization times (Fig. 2 orange line). Therefore, we argue that the plunging region can accelerate electrons locally, forming a power-law distribution that will not have time to be thermalized by protons.

2.3 Electron–electron collisions

A pure power-law distribution of electrons will interact via Coulomb collisions, eventually forming a pure thermal distribution if allowed to evolve freely (Nayakshin & Melia 1998). Lower energy electrons thermalize first, forming a hybrid thermal/non-thermal population at intermediate evolution times. If non-thermal electrons are continuously injected, as Section 2.2 showed is possible in the plunging region, the electron distribution will reach some equilibrium of non-thermal and thermal populations. We model this hybrid distribution as a thermal Maxwell–Jüttner distribution up to a transition Lorentz factor γ_1, where the distribution becomes a power law. A non-thermal electron with Lorentz factor γ will interact with the thermal bulk on the energy loss time-scale $t_{\text{coll}}^{ee}(\gamma) \equiv 1/\nu_\epsilon^{ee}(\gamma)$. The energy loss rate is given by

$$\nu_\epsilon^{ee}(\gamma) = \left[\psi(x^{ee}) - \psi'(x^{ee})\right] \frac{16\sqrt{\pi}e^4 \ln\Lambda\, n_0}{m_e^2 c^3 \beta^3}, \tag{7}$$

where $\beta = \sqrt{1 - 1/\gamma^2}$ and $\psi(x)$ is the lower incomplete Gamma function (Spitzer 1956). The kinetic ratio $x^{ee} = \beta^2/(2\theta_e)$. For an electron temperature of 10^9 K, a particle with a Lorentz factor of 2.0 has an energy loss time-scale of 10^{-6} s, about 0.002 times the infall time-scale (Fig. 2 purple). We therefore cannot neglect electron–electron collisions, especially at lower electron energies.

Though non-thermal electrons will also collide with thermal protons over the corresponding electron–proton energy loss time-scale, this time-scale will be larger than the thermalization time-scale discussed in Section 2.1. We will therefore ignore interactions between non-thermal electrons and thermal ions.

2.4 Importance of radiative cooling

High-energy electrons cool rapidly due to either synchrotron or inverse Compton cooling. In our model, the cooling time $t_{\text{cool}}(\gamma)$ is set

by either synchrotron or inverse Compton cooling, depending on the ratio U_B/U_{ph}, where $U_B = B_r^2/8\pi$ is the magnetic energy density and $U_{ph} = L/(4\pi c \, r_{\rm ISCO}^2)$ is the energy density in the ambient photons, assumed to come from the disc such that $L = 0.1 \, L_{\rm Edd}$, where $L_{\rm Edd} = 4\pi GMm_pc/\sigma_T = 1.26 \times 10^{39}$ erg s^{-1}. If $U_B/U_{ph} > 1$, then the cooling time is set to the time it takes for an electron to lose half its energy due to synchrotron radiation (Rybicki & Lightman 1979):

$$t_{\rm sync}(\gamma) = \frac{5.1 \times 10^8}{\gamma B_r^2}. \tag{8}$$

In using the above equation, we assume that the particle is moving in gyro-orbits around the dominant magnetic field B_r, with a pitch-angle $\alpha = \pi/2$. If on the other hand $U_B/U_{ph} < 1$, the cooling time is set to the inverse Compton cooling time, assumed to take the form

$$t_{\rm IC}(\gamma) = \frac{U_B}{U_{ph}} t_{\rm sync}(\gamma). \tag{9}$$

Notice that equations (8) and (9) are valid only for ultra-relativistic particles. As such, we ignore cooling for electrons below a minimum Lorentz factor $\gamma_{\rm min} = 2$, since below this Lorentz factor the cooling rate decreases rapidly.

The cooling times decrease for larger Lorentz factors, with values at the minimum Lorentz factor two orders of magnitude smaller than the electron–electron collision time, and five orders of magnitude smaller than the infall time-scale (Fig. 2 magenta). The electrons in the plunging region therefore have time to radiate before disappearing beyond the event horizon.

We show the relevant time-scales of the plunging region in Fig. 2 for models with different black hole spin a and accretion efficiencies $\Delta\epsilon$ resulting from different magnetic field strengths. At a radius of $r = 1.58 \, r_g$, all models satisfy the ordering

$$t_{\rm accel} \ll t_{\rm cool}(\gamma) \ll t_{\rm coll}^{ee}(\gamma) \ll t_{\rm infall} \lesssim t_{\rm therm}^{ei} \tag{10}$$

for $\gamma \geq \gamma_1$. We will use this ordering to motivate our model for the plunging region's hybrid thermal/non-thermal electron distribution.

3 MULTIZONE EQUILIBRIUM MODEL

In this section, we present a model for the electron distribution in the plunging region, motivated by the properties outlined in Section 2. We will assume that non-thermal electrons are continuously injected by local processes such as magnetic reconnection or turbulence, which then partially thermalize via electron–electron collisions. We further assume that the hybrid thermal/non-thermal electron distribution reaches a steady state at each radius, matching the losses due to radiation with the heating due to magnetic dissipation. Next, we describe the assumptions that allow us to fully constrain this hybrid electron distribution's form.

3.1 Initial electron distribution

Because the advection time-scales are much longer than the particle acceleration time-scales (Fig. 2), we assume that the initial (pre-thermalization) electron population at each radius is a pure power-law distribution: $f_{\rm PL,0}(\gamma) = A_0\gamma^{-p}$ for $1 \leq \gamma \leq \gamma_2$, where γ_2 is a high-energy cut-off. The high-energy cut-off at each radius is set to

$$\gamma_2(r) = \gamma_c(r) = 4\sigma_e(r), \tag{11}$$

where $\sigma_e = B_r^2(r)/(4\pi n_0 m_e c^2)$ is the (cold) electron magnetization (Werner et al. 2018). The power-law index p is also set by Werner et al. (2018)'s prescription (equation 6), increased by 1 to account for cooling (Blumenthal & Gould 1970). Requiring the distribution

to be normalized to n_0 sets the constant A_0. All together, the initial distribution reads

$$f_{\rm PL,0}(\gamma) = \frac{n_0(p-1)}{1-\gamma_2^{1-p}} \, \gamma^{-p} \quad 1 \leq \gamma \leq \gamma_2. \tag{12}$$

Electron–electron Coulomb collisions will partially thermalize this initial power-law distribution. Radial profiles for the high-energy cut-off γ_2 and the power-law index p in the fiducial model are given in Fig. 3.

3.2 Steady-state electron distribution

Some of the injected power-law electrons will interact with each other via Coulomb collisions, creating a thermal distribution below some Lorentz factor γ_1 (Section 2.3). The resulting hybrid thermal/non-thermal electron distribution continuously gains more non-thermal electrons due to the injection process and loses non-thermal electrons to the thermal bulk, radiating energy. We approximate these rapid processes with a steady-state electron distribution comprising a Maxwell–Jüttner thermal distribution $f_{\rm MJ}$ and a power-law distribution $f_{\rm PL}(\gamma)$ for $\gamma_1 \leq \gamma \leq \gamma_2$.

The thermal electron distribution $f_{\rm MJ}$ is fully described by two variables: its normalization and its temperature T_e. We fix the normalization of the thermal distribution to the number density n_0, assuming that the number of non-thermal electrons is negligible compared to the thermal electrons. Explicitly, the thermal distribution reads

$$f_{\rm MJ}(\gamma, \, \theta_e, \, n_0) = n_0 \frac{\gamma^2\beta}{\theta_e K_2(1/\theta_e)} e^{-\gamma/\theta_e}, \tag{13}$$

where K_2 is the modified Bessel function of the second kind. The electron temperature $T_e = \theta_e m_e c^2/k_B$ is set by the model assumptions outlined below.

The non-thermal electrons are described as a power-law between a minimum Lorentz factor γ_1 and a high-energy cut-off γ_2, with a power-law index $p_{\rm eff}$ and a normalization $A_{\rm PL}$:

$$f_{\rm PL}(\gamma) = A_{\rm PL}\gamma^{-p_{\rm eff}} \quad \gamma_1 \leq \gamma \leq \gamma_2. \tag{14}$$

We will now outline how our model determines the variables γ_1, $A_{\rm PL}$, $p_{\rm eff}$, and T_e.

3.2.1 Determining γ_1

The minimum Lorentz factor γ_1 of the non-thermal distribution is set at the energy where collisions and cooling balance. At γ_1, the energy loss time-scale $t_{\rm coll}^{ee}$ (equation 7) equals the cooling time $t_{\rm cool}$:

$$t_{\rm coll}^{ee}(\gamma_1) = t_{\rm cool}(\gamma_1). \tag{15}$$

Here, the cooling time $t_{\rm cool}$ is set to the minimum of the synchrotron and inverse Compton cooling times (equations 8 and 9). We enforce the lower bound $\gamma_{1,\rm min} = \gamma_{\rm min} = 2.0$ to model the inefficiency of cooling at low energies. We also require that $\gamma_1 > \gamma_{\rm threshold}(T_e)$, where the threshold Lorentz factor $\gamma_{\rm threshold}$ is where the energy loss frequency (equation 7) is zero for a given temperature. A power-law electron with a Lorentz factor below $\gamma_{\rm threshold}$ would increase in energy due to collisions with the thermal bulk. Imposing the requirement that the power-law start at Lorentz factors greater than the threshold Lorentz factor means that γ_1 will always be to the right of the thermal peak, thereby avoiding getting trapped at solutions with $\gamma_1 \rightarrow 1$.

Often, the cooling times are shorter than the energy loss times for all values of Lorentz factor. In this case, collisions are never
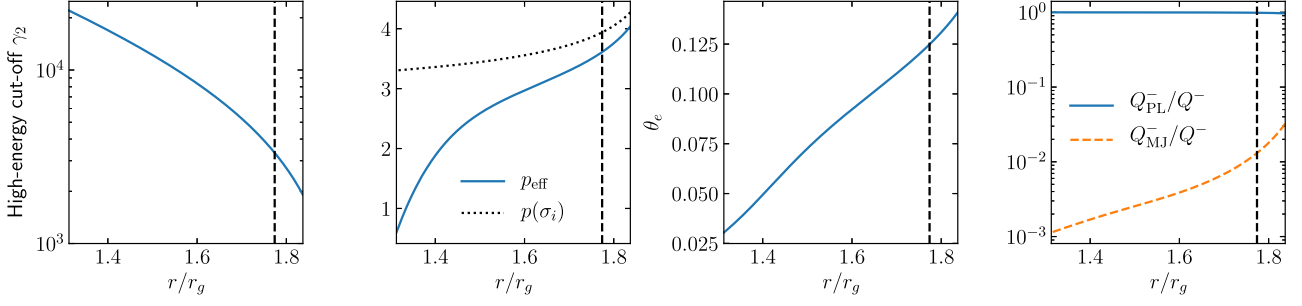
Figure 3. Radial profiles of the electron distribution function model properties for fiducial parameters $a = 0.95$ and $\Delta\epsilon = 1.04$. From left to right: the high-energy Lorentz factor cut-off of the power law γ_2, the electron power-law index, the thermal electron temperature $\theta_e = k_B T_e/m_e c^2$, and the fraction of the total cooling rate Q_- from the power-law and thermal component. The vertical dashed line shows the location of the half-light radius.

important for the non-thermal electrons (Fig. 2). However, it is still important to maintain a thermal population of electrons to provide the bulk of the density in the plunging region. When no solution to equation (15) exists, we set $\gamma_1 = \max(\gamma_{1,\text{threshold}}, \gamma_{\min})$.

3.2.2 Determining A_{PL}

The power-law normalization A_{PL} is set by requiring continuity of the thermal and non-thermal electrons at γ_1:

$$f_{\text{MJ}}(\gamma_1) = f_{\text{PL}}(\gamma_1). \tag{16}$$

3.2.3 Determining p_{eff}

The power-law index p_{eff} of the steady-state non-thermal distribution is calculated by assuming that none of the highest energy particles are thermalized by Coulomb collisions; that is,

$$f_{\text{PL},0}(\gamma_2) = f_{\text{PL}}(\gamma_2). \tag{17}$$

We use an effective power-law index because high-energy particles collide more slowly than lower energy particles, resulting in a power-law index that decreases over time (Nayakshin & Melia 1998). Using the power-law index from PIC simulations would underestimate the total power law. Our formulation assumes that the initial power law is continually replenished by *in situ* particle acceleration, so the impact of cooling is primarily in the radiation rather than the dynamics. The difference between p_{eff} and p is largest close to the event horizon (Fig. 3). Fig. 4 shows how the final power-law distribution (blue solid line) differs from the initial power-law distribution (purple dashed line).

Combining equations (12) and (17) yields an expression for p_{eff}:

$$p_{\text{eff}} = \frac{\log\left[f_{\text{PL},0}(\gamma_2)/f_{\text{MJ}}(\gamma_1)\right]}{\log\left[\gamma_1/\gamma_2\right]}. \tag{18}$$

3.2.4 Determining T_e

The temperature T_e of the thermal electrons is set by requiring a steady state that balances energy lost to radiation with energy dissipated by magnetic torques. We obtain the volume heating rate Q_+ from the accretion efficiency $\Delta\epsilon$ given by the Gammie (1999) model, assuming that dissipation occurs evenly throughout the plunging region's volume:

$$Q_+ = \delta_e \frac{\Delta\epsilon\, L_{\text{Edd}}}{V_{\text{PR}}}, \tag{19}$$
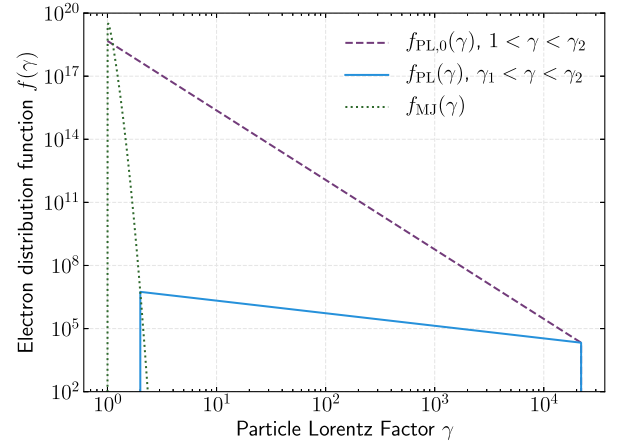
Figure 4. The effective power-law index p_{eff} is calculated from the initial power-law distribution $f_{\text{PL},0}$ by assuming that both power laws have the same value at the high-energy cut-off γ_2 (equation 17). This sample electron distribution was calculated for fiducial parameters close to the event horizon at a radius $r = 1.31\, r_g$, where $p = 3.3$ (purple dashed line) and $p_{\text{eff}} = 0.6$ (blue solid line). For radii closer to the ISCO, the difference between $f_{\text{PL},0}$ and f_{PL} is not so pronounced. The thermal distribution is also shown for reference (green dotted line).

where $V_{\text{PR}} = 4\pi(r_{\text{ISCO}}^3 - r_{\text{EH}}^3)/3$ is the (Newtonian) volume of the plunging region. The fraction of dissipated energy δ_e that goes into electrons is set at a constant value of 0.5, as motivated by PIC simulations of the energy partition in an electron-ion plasma with magnetizations close to 1 (Werner et al. 2018; Zhdankin et al. 2019). The remainder $1 - \delta_e$ fraction of dissipated energy heats the ions, which do not radiate.

The total cooling rate Q_- sums the bremsstrahlung cooling rate $Q_{-,\text{MJ}}$ from the thermal electrons with the inverse Compton or synchrotron cooling rate from the non-thermal electrons. To account for additional scattering, the non-thermal cooling rate $Q_{-,\text{PL}}$ is set to the non-thermal emitted power $\mathcal{P}_{-,\text{PL}}$ decreased by a factor of $\tau_e = n_0\sigma_T H = n_0\sigma_T(H/r)r$, such that $Q_{-,\text{PL}} = \mathcal{P}_{-,\text{PL}}/\tau_e$. This additional factor estimates how many of the synchrotron/IC photons would escape the plunging region without additional scattering, which is important since $\tau_e \gtrsim 1$. This choice is motivated by Monte Carlo simulations of an isotropic sphere of gas with photons packets initialized evenly throughout the sphere. These simulations show that about $1/\tau_e$ of the electrons escape with no scattering. The remaining $1 - 1/\tau_e$ fraction of photons will Compton scatter off of the thermal/non-thermal electrons, heat the gas, and re-energize

non-thermal electrons. The equation for steady state thus reads

$$Q+ = Q_- = Q_{-,\text{MJ}} + Q_{-,\text{PL}}. \tag{20}$$

The non-thermal emissivity $\mathcal{P}_{-,\text{PL}}$ is calculated by integrating the Larmor formula for power emitted per electron over frequency ω, the power-law electron distribution $f_{\text{PL}}(\gamma)$, and solid angle. In integrating over solid angle Ω, we assume an isotropic distribution of pitch-angles α. The resulting power lost per unit volume is given by

$$\mathcal{P}_{-,\text{PL}}^{\text{sync}} = \int \, d\Omega \, d\omega \, d\gamma \, f_{\text{PL}}(\gamma) \frac{2e^4 B_r^2 \gamma^2 \beta^2 \sin^2 \alpha}{3m_e^2 c^3} \tag{21}$$

$$= \frac{16\pi e^4 B_r^2}{9m_e^2 c^3} \int_{\gamma_1}^{\gamma_2} (\gamma^2 - 1) A_{\text{PL}} n_0 \gamma^{-p_{\text{eff}}} d\gamma. \tag{22}$$

If inverse Compton dominates, the emissivity is set to $\mathcal{P}_{-,\text{PL}}^{\text{IC}} = (U_{ph}/U_B)\mathcal{P}_{-,\text{PL}}^{\text{sync}}$.

We describe the cooling due to thermal particles in the plunging region as saturated Comptonized bremsstrahlung. Because the optical depth is of order 1 and the Compton y parameter is much greater than 1, the bremsstrahlung is amplified by repeated inverse Compton scatterings. The resulting emissivity is

$$Q_{-,\text{MJ}} = A(n_0, T_e)\epsilon_{\text{ff}}(n_0, T), \tag{23}$$

where $A(n_0, T_e) = 0.74[\ln(2.25/x_{coh})]^2$ is an approximate amplification factor due to repeated inverse Compton scattering, $x_{coh} = 2.4 \times 10^{17}(m_e n_0)^{1/2} T_e^{-9/4}$ and $\epsilon_{ff}(n_0, T) = 1.68 \times 10^{-27} T_e^{1/2} n_0^2$, is the standard bremsstrahlung emissivity (Rybicki & Lightman 1979).

Because the energy loss collision times (equation 7) assume a non-relativistic thermal bulk, we put an upper limit on T_e at the temperature T_{max} where setting $\nu_\epsilon^{ee}(x_c^{ee}) = 0$ would require a particle velocity greater than the speed of light. This maximum temperature is $T_{\text{max}} = 3 \times 10^9$ K.

Equations (15), (17), (16), and (20) are solved iteratively at each radius using Brent's method to obtain $\gamma_1(r)$, $p_{\text{eff}}(r)$, $A_{\text{PL}}(r)$, and $T_e(r)$.

4 RESULTS

4.1 High-spin, highly magnetized case

To illustrate the model, we examine the fiducial case $a = 0.95$ and $\Delta\epsilon = 1.04$, which corresponds to $F_{\theta\phi} = 6.0$ and magnetic flux a factor of 2 below the saturation value for a magnetically arrested disc (Avara et al. 2016). The hierarchy of time-scales for this fiducial model justifies the assumptions outlined in Section 2. For this set of parameters, γ_1 always hits the lower bound $\gamma_{1,\text{min}} = 2.0$. The equilibrium electron temperature θ_e decreases from 0.14 (8.9×10^8 K) at the ISCO to 0.03 (1.9×10^8) K at the event horizon (Fig. 3). These temperatures are roughly consistent with the inner disc temperatures in two-temperature GRMHD simulations (Liska et al. 2022). The temperature decreases towards the event horizon because of the increase in γ_2, decreasing the power law's overall normalization and shifting the temperature lower because of the continuity requirement (equation 16). The decoupling of electrons and protons happens very close to the ISCO, at 1.82 r_g, meaning that almost the entire plunging region has decoupled. The cooling rate is dominated by non-thermal synchrotron emission, with thermal cooling representing $\lesssim 1$ per cent of the cooling rate at the ISCO and 0.1 per cent at the event horizon (Fig. 3). This increase in the fraction of cooling from non-thermal electrons is again driven by the increase in γ_2, which is set by the background magnetic field and gas density.

The total spectrum, shown in Fig. 5, consists of three parts: the plunging region's non-thermal electrons (blue solid line), the plunging region's thermal electrons (green dotted line), and the thin
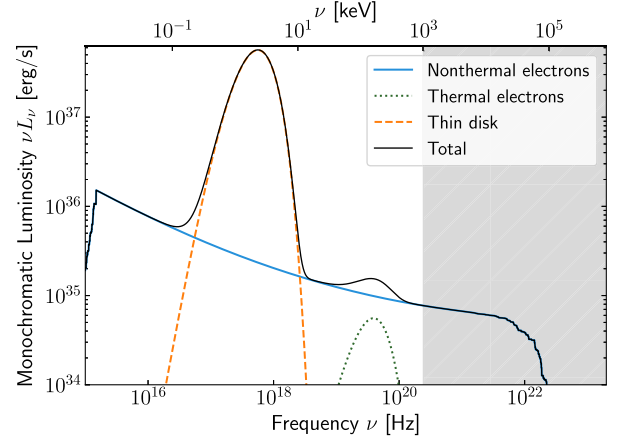

Figure 5. Spectrum for the fiducial model parameters $a = 0.95$ and $F_{\theta\phi} = 6.0$ at an inclination of $60°$. The thin disc emission (dashed orange line) peaks around a few keV. The non-thermal electrons' radiation (solid blue line) extends from 10 eV to 0.1 GeV, although emission beyond 1 MeV (grey region) may be impacted by pair creation. The thermal electrons in the plunging region create a small excess at around 10 keV (dotted green line).

disc's spectrum (orange dashed line). The spectrum is calculated with redshifts obtained by ray tracing the plunging region-disc system with the code `geokerr` to a camera inclined at $i = 60°$ to the black hole and disc angular momentum vector (Dexter & Agol 2009). The gas is assumed to have a four-velocity given by the Gammie (1999) model within the plunging region and a purely azimuthal, Keplerian velocity in the disc body. The power-law intensities $I_{\nu, \text{PL}, ij} = P_{\nu, \text{PL}, ij} H/(4\pi)$ at a camera pixel with position i and j in the $x-$ and $y-$directions are calculated by assuming a hybrid electron distribution at the radius r_{ij} where the ray-traced photon hits the plunging region mid-plane. The power-law distribution is $P_{\nu,\text{PL},ij} = A_{ij}\nu^{-s_{ij}}$ between the characteristic synchrotron frequencies $\nu_{1, ij}$ and $\nu_{2, ij}$ for electrons with Lorentz factors $\gamma_{1, ij}$ and $\gamma_{2, ij}$. That is, $\nu_1 = \nu_0\gamma_{1,ij}^2$ and $\nu_2 = \nu_0\gamma_{2,ij}^2$, where $\nu_0 = 3e|B_r|/(4\pi m_e c)$. The power-law slope is $s_{ij} = (p_{\text{eff}, ij} - 1)/2$. The constant A_{ij} is set by requiring that $\int P_{\nu,\text{PL},ij} d\nu = Q_{-,\text{PL},ij}$. The emission from the thermal plunging region electrons is in the Comptonized Wien regime, such that $I_{\nu,\text{MJ},ij} = I_\nu^W(T_{ij})e^{-\alpha_{ij}}$, where T_{ij} is the thermal electron temperature at r_{ij}, $I_\nu^W(T_{ij}) = 2h\nu^3/c^2 e^{-kT_{ij}/h\nu}$ is the Wien intensity, and $e^{-\alpha_{ij}}$ is the Compton saturation factor. The Compton saturation factor is determined by setting the frequency-integrated intensity equal to the isotropic thermal Comptonized bremsstrahlung emissivity: $I^W(T_{ij})e^{-\alpha_{ij}} = Q_{-,\text{MJ}}H/4\pi$. Luminosities are obtained by summing over 64×64 camera pixels: $L_\nu = 4\pi \Delta\alpha\Delta\beta\sum_{ij}I_{\nu, ij}$, where $\Delta\alpha = \Delta\beta = 0.125r_g$ are the pixel widths. The disc spectrum is calculated by assuming a blackbody with a radially dependent temperature extending from the ISCO to 10^{10} cm (Frank, King & Raine 2002):

$$T(r) = \left(\frac{3GM\dot{M}}{8\pi\sigma r^3}\frac{\mathcal{Q}}{\mathcal{B}\mathcal{C}^{1/2}}\right)^{1/4}, \tag{24}$$

where $\mathcal{B}$, $\mathcal{C}$, and $\mathcal{Q}$ are relativistic corrections (Novikov & Thorne 1973; Page & Thorne 1974).

Several features of the spectrum in Fig. 5 stand out. First, emission from the non-thermal plunging region electrons dominates the emission above 10 keV and produces an observable high-energy power-law tail. The power law has a relatively flat slope past 200 keV, a feature that is difficult to produce through thermal Comptonization (Coppi 1999). This power law cuts off at a little less than 100
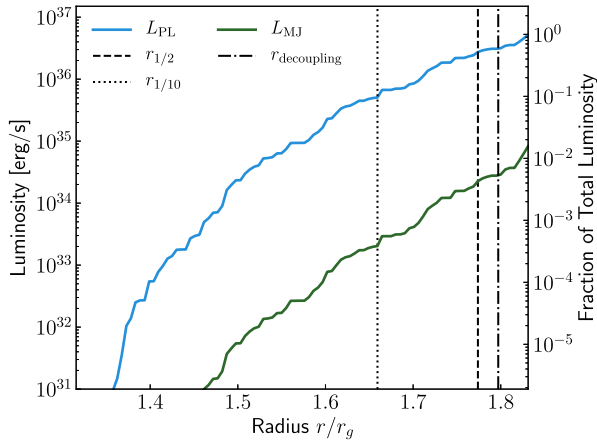
Figure 6. Portion of the fiducial model's observed frequency-integrated luminosity originating between the event horizon and a radius r for an inclination angle of $60°$. Emission from the plunging region's non-thermal electrons (blue) dominates over the plunging region's thermal electrons (green). 10 per cent of the luminosity comes from $r < r_{1/10} = 1.66 r_g$ (dotted line), while 50 per cent comes from $r < r_{1/2} = 1.77 r_g$ (dashed line). The vertical dash–dotted line shows the decoupling radius.

MeV, though above 1 MeV pair production could become important (grey region). The total luminosity from the power law across all frequencies is 6.1 per cent of the disc luminosity. This fraction decreases to 1.7 per cent if non-X-ray frequencies below 1 keV are excluded. Excluding luminosity from the pair-emitting frequency range above 1 MeV further decreases the fraction to 1.3 per cent. The non-thermal power-law electrons dominate emission from the plunging region, with a luminosity 63, 15, or 12 times that of the thermal plunging region electrons for all frequencies, frequencies above 1 keV, and frequencies between 1 keV and 1 MeV, respectively.

Most of the observed luminosity comes from radii close to the ISCO, as shown in Fig. 6. This figure shows the amount of observed luminosity that originates from between the event horizon and a radius r. We define the half-light radius $r_{1/2}$ as the location within which 50 per cent of the light from the plunging region has been emitted; analogously, $r_{1/10}$ is where 10 per cent of the light has been emitted. For this fiducial case with the ISCO at $r = 1.94 r_g$, 50 per cent of the light comes from $r > 1.77 r_g$ and 90 per cent comes from $r > 1.66 r_g$.

The emission depends on the spin and the inclination of the disc-plunging region system. The inclination of the disc with respect to an observer changes the effective observed area, an effect that goes as $\cos i$, where i is the angle between the black hole spin axis and the lines of sight. Relativistic beaming effects have the opposite trend with inclination angle; radiation from relativistically moving gas is beamed into the plane of motion, leading to a higher luminosity for larger inclination angles. In the plunging region, beaming effects dominate, resulting in a factor of 100 increase in power-law luminosity from $i = 0°$ ($L_{PL} = 5 \times 10^{35}$ erg s^{-1}) to $i = 90°$ ($L_{PL} = 6 \times 10^{37}$ erg s^{-1}) for $a = 0.95$. Power-law emission for $a = 0.5$ is roughly constant over inclination angle, with $L_{PL} \sim 2 - 3 \times 10^{36}$ erg s^{-1}. Beaming effects no longer dominate for the smaller spin because the fluid Lorentz factor is smaller due to a larger r_{ISCO}. The blackbody disc's peak temperature depends on the location of the ISCO, which is set by the black hole spin and decreases by a factor of about three from a non-spinning to a maximally spinning black hole (Cunningham 1975; Li et al. 2005). The disc emission is non-monotonic as a function of inclination angle, peaking around $60°$, where area projection effects start to dominate over Doppler
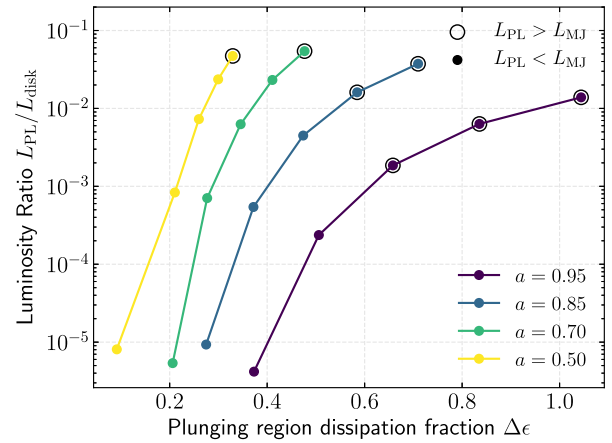

Figure 7. Frequency-integrated luminosity in X-rays (1 keV $< \nu <$ 1 MeV) in predicted power law compared to the thermal blackbody disc for different model parameters, assuming an inclination angle $i = 60°$. Models where non-thermal electron emission dominates over thermal electron emission, satisfying $L_{PL} > L_{MJ}$, are marked with large black circles.

effects. The peak disc emission is a factor of two larger than at $i = 0°$ for $a = 0.95$, and a factor of 1.7 larger for $a = 0.5$. As a result, L_{PL}/L_{disc}(1 keV $< \nu <$ 1 MeV) for $a = 0.95$ increases from 0.002 at $i = 0°$ to 0.17 at $i = 85°$, whereas for $a = 0.5$ it increases from 0.055 at $i = 0°$ to 0.09 at $i = 85°$, with a minimum of 0.042 at $i = 45°$.

4.2 Parameter space

Fig. 7 shows the power law to disc luminosity fraction as a function of plunging region dissipation and black hole spin. For $i = 60°$, the plunging region can emit up to 1 per cent of the accretion disc luminosity for a high-spin black hole, and even higher for lower spin black holes. At constant spin, discs with less magnetic torque at the ISCO and hence a lower accretion efficiency $\Delta\epsilon$ have less non-thermal luminosity because weaker magnetic fields lead to less efficient cooling of high-energy particles, whereas the thin disc emission is constant with $\Delta\epsilon$. At fixed $\Delta\epsilon$, lower black hole spins lead to a more visible power law because the plunging region extends to larger radii, increasing the magnitude of the non-thermal plunging region luminosity and decreasing the disc luminosity. For $\Delta\epsilon \approx 0.4$, the power law's X-ray luminosity increases by a factor of 400, from 10^{33} erg s^{-1} for $a = 0.95$ to 4×10^{35} erg s^{-1} for $a = 0.70$. This increase is due to a combination of a larger area radiating 90 per cent of the emission and redshifts closer to unity for smaller spins. The thin disc's X-ray luminosity decreases for decreasing spin by a factor of 10, from 10^{38} to 10^{37} erg s^{-1}. These combined effects explain why L_{PL}/L_{disc} is a factor of 4000 different for the same magnetization.

Our model demonstrates two regimes for the plunging region X-ray emission: one where non-thermal electrons dominate and one where thermal electrons dominate. For fixed spin, weaker magnetic fields lead to less cooling by non-thermal electrons and thus require more thermal cooling and higher thermal temperatures to balance the total heating rate. Higher thermal temperatures and a less prominent power law lead to a significant decrease in L_{PL}/L_{MJ} with decreasing accretion efficiency. Non-thermal electrons dominate only at the highest disc magnetizations because particle acceleration requires strong magnetic fields. For less strongly magnetized discs, thermal electrons dominate the plunging region emission; in this regime, we might expect the observed power law to come from thermal electrons with a rapidly increasing temperature rather than non-
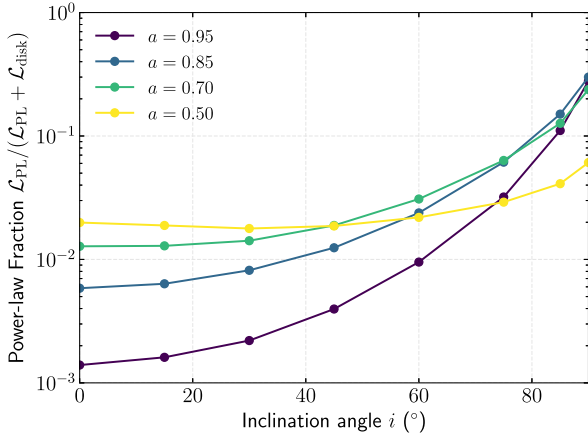
Figure 8. PLF (equation 25) as a function of inclination angle. Calculated from the most strongly magnetized plunging region parameters such that non-thermal plunging region emission dominates thermal plunging region emission.

thermal electrons (Zhu et al. 2012). Fig. 7 marks the regime where non-thermal electrons dominate with black circles around the coloured markers.

To facilitate comparison with observations, we show our model's predictions for the power-law fraction (PLF) as a function of inclination angle and spin in Fig. 8. The PLF is defined as

$$\mathrm{PLF} = \frac{\mathcal{L}_{\mathrm{PL}}}{\mathcal{L}_{\mathrm{PL}} + \mathcal{L}_{\mathrm{disc}}}, \tag{25}$$

where $\mathcal{L}_{\mathrm{PL}} = L_{\mathrm{PL}}(1 \text{ keV} < \nu < 100 \text{ keV})$ is the power-law luminosity in the X-rays and $\mathcal{L}_{\mathrm{disc}} = L_{\mathrm{disc}}(0.001 \text{ keV} < \nu < 100 \text{ keV})$ is the disc luminosity over a wide range of frequencies, to avoid cutting off low-spin blackbody emission that peaks at ~ 1 keV (Dunn et al. 2010; Muñoz-Darias et al. 2013). For the high-spin case, the PLF is almost the same as $L_{\mathrm{PL}}/L_{\mathrm{disc}}(1 \text{ keV} < \nu < 1 \text{ MeV})$ because $L_{\mathrm{PL}} \ll L_{\mathrm{disc}}$. For lower spins, the PLF is lower than $L_{\mathrm{PL}}/L_{\mathrm{disc}}(1 \text{ keV} < \nu < 1 \text{ MeV})$ by a factor of 2–3 because of the change in denominator. The parameters in Fig. 8 are the most strongly magnetized discs where the non-thermal emission dominates thermal emission from the plunging region; for the least magnetized cases, the PLF is less than 10^{-3} (not shown) and thermal plunging region electrons would significantly change the shape of the emission above 10 keV. Overall, the PLF calculated from the model lies between 10^{-3} and 0.3, values consistent with observations of the soft state (Dunn et al. 2010).

5 DISCUSSION

5.1 Application to astrophysical systems

Our model broadly agrees with observations of X-ray binaries in the soft state. The soft state usually exhibits a photon index $\Gamma \gtrsim 2$ (Remillard & McClintock 2006), corresponding to model fits with an electron power-law index $p \gtrsim 3$. The model's most strongly magnetized parameters give an electron power-law index of 3–4 (Fig. 3), which increases for decreasing magnetization. The soft state's gamma-ray tail has luminosities of the order of 10^{35}–10^{37} erg s^{-1} above 50 keV (Grove et al. 1998). Our model finds power-law luminosities above 50 keV between 10^{34}–10^{37} erg s^{-1}, within the same order of magnitude. Calculations from observations find that the PLF varies between 10^{-3} and 0.2 in the soft state of XRBs (Dunn et al. 2010), which agrees well with the values found

from our model (Fig. 8). As yet, trends of the PLF with inclination angle and spin cannot be found from observations (Muñoz-Darias et al. 2013). Testing our predictions concretely against observations will require less uncertainty in the PLF.

The power-law emission in our model comes from synchrotron emission, whereas typical models for the power law assume inverse Compton scattering of blackbody disc photons off non-thermal particles (Gierliński et al. 1999; McConnell et al. 2002). Our model therefore predicts more strongly polarized emission for the soft state's emission above 10 keV than other models where inverse Compton scattering dominates. Current polarization measurements set an upper limit of 70 per cent for Cyg X-1's 0.4–2 MeV emission in the soft state (Rodriguez et al. 2015), which does not constrain the radiation mechanism.

The hard state of XRBs such as Cyg X-1 shows an excess above 400 keV that fits well to a hybrid thermal/non-thermal model with a power-law electron distribution index between 3.5 and 5 (McConnell et al. 2000). The non-thermal electrons in that model could also be accelerated by turbulence or magnetic reconnection. If the hierarchy of time-scales satisfies equation (10), the multizone equilibrium model presented in Section 3 could be adapted to a geometry relevant to the hard state.

5.2 Model limitations

Many of our model assumptions were motivated by GRMHD simulations. Our finding that ions and electrons decouple in the plunging region is consistent with estimates of the thermalization time from single-temperature, ideal GRMHD simulations (Zhu et al. 2012). In fact, the decoupling region could extend even outside the ISCO. The Gammie (1999) model artificially sets the radial velocity to zero at the ISCO, forcing a thin disc at $r > r_{\mathrm{ISCO}}$, whereas the thin disc could in principle thicken at larger radii depending on the dominance of Coulomb collisions. For simplicity, in our model, the ion temperature and thus the ratio H/R was discontinuous at the ISCO. This discontinuity is not present in full 3D GRMHD simulations; instead, a transition region forms between a thin disc and the hot flow (Hogg & Reynolds 2018; Liska et al. 2022). Such a transition region would likely result in a less distinct bump from the thermal electrons in the plunging region. GRMHD simulations also motivate magnetic reconnection as an important dissipation mechanism, demonstrating hallmarks of reconnection such as current sheets and plasmoids throughout a magnetically dominated disc (Ripperda et al. 2022; Scepi, Dexter & Begelman 2022). Our prescription for γ_2 and p does not include the impact of particle anisotropy or magnetic guide field on the electron distribution (Comisso, Sobacchi & Sironi 2020; Werner & Uzdensky 2021), which could alter the observed spectrum. Including a guide field tends to steepen p and decrease γ_2 for a pair plasma (Werner & Uzdensky 2017, 2021). Pitch-angle anisotropy in a pair plasma can also lead to temperature anisotropy for the thermal bulk (Comisso & Sironi 2019; Comisso et al. 2020), which could affect radiation from the thermal plunging region electrons. Unlike GRMHD simulations, our model does not include vertical structure and we assumed a constant $H/R = 1$ and a uniform distribution of the dissipation throughout the plunging region volume. The vertical structure would presumably lead to a dense equatorial region with more optically thin upper parts of the plunging region. We also assume uniform dissipation such that $Q_+ \propto \rho$, as commonly done in disc atmosphere models (Davis & Hubeny 2006).

For simplicity, we did not include full radiative transport in our model. Instead, we assumed that the thermal plunging region electrons cooled solely through thermal bremsstrahlung, neglecting

thermal synchrotron radiation because the average Lorentz factor of the thermal particles was less than 2 (i.e. temperatures less than $\sim10^9$ K). We also neglect synchrotron self-absorption, since this effect is only important for frequencies below $\sim10^{15}$ Hz (Wardziński & Zdziarski 2000), outside the range we consider. We neglect cyclotron radiation for the same reason. We restrict the observed radiation from the non-thermal electrons to be either from synchrotron radiation or from inverse Comptonization of soft disc photons, i.e. we neglect synchrotron self-Compton emission (SSC). Neglecting SSC does not result in large errors for small optical depth and spectral index >1, where synchrotron emission dominates over SSC (Wardziński & Zdziarski 2001). We also do not consider synchrotron and inverse Compton processes simultaneously; instead, we assume one or the other dominates. We also assume a simple thermal + power-law electron distribution function, whereas Fokker–Planck models evolving a power-law electron distribution thermalizing under electron–electron collisions show a more complicated structure (Nayakshin & Melia 1998). Although pair production could become important in this regime, it remains unclear how pair-regulated reconnection would change when synchrotron losses are included (Mehlhaff et al. 2021). We note that Compton reflection off the cold disc could increase the luminosity above 10 keV by order unity for sandwich-type models (Zdziarski & Gierlinski 2004). Including Compton reflection of the plunging region radiation off the cold disc could also increase the high-energy luminosity and lead to higher PLFs. More detailed modelling of reflection features such as the Fe Kα emission line is beyond the scope of this work.

6 CONCLUSIONS

We have presented a semi-analytic model for the soft state of XRBs, where the high-energy power-law tail is produced by non-thermal electrons in the plunging region. We demonstrated the feasibility of having non-thermal electrons in the plunging region by examining the hierarchy between electron–proton thermalization time, electron–electron collision time, electron cooling time, electron acceleration time, and the infall time (Section 2, Fig. 2). Using an analytic dynamical background and the results of PIC simulations of magnetic reconnection, we constructed a steady-state model for the electron distribution function at each radius in the plunging region (Section 3). The non-thermal electrons in this model produce an observable power law from 10 to 1000 keV with a photon spectral index $\Gamma \gtrsim 2$ (Fig. 5). By exploring the model parameter space, we show that plunging region emission from non-thermal electrons dominates over thermal electrons for strongly magnetized models and vice versa for less strongly magnetized models, suggesting a Zhu et al. (2012)-type model. We found fractions of power law to total X-ray luminosity (PLF) consistent with observations for all values of spin (Fig. 7). We predict an increase in the observed PLF with inclination angle (Fig. 8). Although the PLF in our model is consistent with observational values, testing the trend with inclination angle and spin will require more observations.

Future work using numerical simulations could explore how and where the decoupling happens, as well as its possible role in spectral state transitions and jet/wind launching.

DATA AVAILABILITY

The simulation data underlying this article will be shared on reasonable request to the corresponding author.

REFERENCES

Agol E., Krolik J. H., 2000, ApJ, 528, 161
Armitage P. J., Reynolds C. S., Chiang J., 2001, ApJ, 548, 868
Avara M. J., McKinney J. C., Reynolds C. S., 2016, MNRAS, 462, 636
Blumenthal G. R., Gould R. J., 1970, Rev. Mod. Phys., 42, 237
Comisso L., Sironi L., 2019, ApJ, 886, 122
Comisso L., Sobacchi E., Sironi L., 2020, ApJ, 895, L40
Coppi P. S., 1999, in Poutanen J., Svensson R., eds, ASP Conf. Ser. Vol. 161 High Energy Processes in Accreting Black Holes. Astron. Soc. Pac., San Francisco, p. 375
Cunningham C. T., 1975, ApJ, 202, 788
Davis S. W., Hubeny I., 2006, ApJS, 164, 530
Dexter J., Agol E., 2009, ApJ, 696, 1616
Dexter J., Blaes O., 2014, MNRAS, 438, 3352
Dunn R. J. H., Fender R. P., Körding E. G., Belloni T., Cabanac C., 2010, MNRAS, 403, 61
Frank J., King A., Raine D. J., 2002, Accretion Power in Astrophysics, 3rd edn. Cambridge Univ. Press, Cambridge
Gammie C. F., 1999, ApJ, 522, L57
Gierliński M., Zdziarski A. A., Poutanen J., Coppi P. S., Ebisawa K., Johnson W. N., 1999, MNRAS, 309, 496
Grove J. E., Johnson W. N., Kroeger R. A., McNaron-Brown K., Skibo J. G., Phlips B. F., 1998, ApJ, 500, 899
Hogg J. D., Reynolds C. S., 2018, ApJ, 854, 6
Li L.-X., Zimmerman E. R., Narayan R., McClintock J. E., 2005, ApJS, 157, 335
Liska M., Musoke G., Tchekhovskhoy A., Porth O., 2022, preprint (arXiv:2201.03526)
McConnell M. L. et al., 2000, ApJ, 543, 928
McConnell M. L. et al., 2002, ApJ, 572, 984
Mehlhaff J. M., Werner G. R., Uzdensky D. A., Begelman M. C., 2021, MNRAS, 508, 4532
Muñoz-Darias T., Coriat M., Plant D. S., Ponti G., Fender R. P., Dunn R. J. H., 2013, MNRAS, 432, 1330
Nayakshin S., Melia F., 1998, ApJS, 114, 269
Noble S. C., Krolik J. H., Hawley J. F., 2009, ApJ, 692, 411
Novikov I. D., Thorne K. S., 1973, Black Holes (Les Astres Occlus). Gordon and Breach Science Publishers, New York, p. 343
Page D. N., Thorne K. S., 1974, ApJ, 191, 499
Penna R. F., McKinney J. C., Narayan R., Tchekhovskoy A., Shafee R., McClintock J. E., 2010, MNRAS, 408, 752
Remillard R. A., McClintock J. E., 2006, ARA&A, 44, 49
Ripperda B., Liska M., Chatterjee K., Musoke G., Philippov A. A., Markoff S. B., Tchekhovskoy A., Younsi Z., 2022, ApJ, 924, L32
Rodriguez J. et al., 2015, ApJ, 807, 17
Rybicki G. B., Lightman A. P., 1979, Radiative Processes in Astrophysics. John Wiley & Sons, Inc., New York
Scepi N., Dexter J., Begelman M. C., 2022, MNRAS, 511, 3536
Shafee R., McKinney J. C., Narayan R., Tchekhovskoy A., Gammie C. F., McClintock J. E., 2008, ApJ, 687, L25
Shakura N. I., Sunyaev R. A., 1973, A&A, 500, 33
Spitzer L., 1956, Physics of Fully Ionized Gases. Interscience Publishers, Inc., New York
Stepney S., Guilbert P. W., 1983, MNRAS, 204, 1269
Wardziński G., Zdziarski A. A., 2000, MNRAS, 314, 183
Wardziński G., Zdziarski A. A., 2001, MNRAS, 327, 351

Werner G. R., Uzdensky D. A., 2017, ApJ, 843, L27

Werner G. R., Uzdensky D. A., 2021, J. Plasma Phys., 87, 905870613

Werner G. R., Uzdensky D. A., Begelman M. C., Cerutti B., Nalewajko K., 2018, MNRAS, 473, 4840

Zdziarski A. A., Gierlinski M., 2004, Prog. Theor. Phys. Suppl., 155, 99

Zdziarski A. A., Grove J. E., Poutanen J., Rao A. R., Vadawale S. V., 2001, ApJ, 554, L45

Zhdankin V., Uzdensky D. A., Werner G. R., Begelman M. C., 2019, Phys. Rev. Lett., 122, 055101

Zhu Y., Davis S. W., Narayan R., Kulkarni A. K., Penna R. F., McClintock J. E., 2012, MNRAS, 424, 2504

This paper has been typeset from a TEX/LATEX file prepared by the author.